Activating inert non-defect sites in Bi catalysts using tensile strain engineering for highly active CO$_2$ electroreduction

Xingbao Chen[1,2,7], Ruihu Lu[2,7], Chengbo Li[3,7], Wen Luo[1]✉, Ruohan Yu[1], Jiexin Zhu[1,2]✉, Lei Lv[1], Yuhang Dai[1], Shanhe Gong[4], Yazhou Zhou[5], Weiwei Xiong[1], Jiahao Wu[1], Hongwei Cai[1], Xinfei Wu[1], Zhaohui Deng[1], Boyu Xing[1], Lin Su[6], Feiyue Wang[1], Feiyang Chao[1], Wei Chen[1], Chuan Xia[3], Ziyun Wang[2]✉ & Liqiang Mai[1]✉

Bi-defect sites are highly effective for CO$_2$ reduction (CO$_2$RR) to formic acid, yet most catalytic surfaces predominantly feature inert, non-defective Bi sites. To overcome this limitation, herein, tensile strain is introduced on wholescale non-defective Bi sites. Under rapid thermal shock, the Bi-based metal-organic framework (Bi-MOF-TS) shows weakened Bi–O bonds and produced tiny Bi clusters. During electrochemical reduction, these clusters create numerous continuous vacancies, inducing weak tensile strain over a large range of surrounding non-defective Bi sites. This strain enhances *OHCO intermediates adsorption and substantially lowers the reaction barrier. As a result, Bi-MOF-TS achieves a faradaic efficiency above 90% across 800 mV potential range, with an impressive formate partial current density of -995 ± 93 mA cm^{-2}. Notably, Bi-MOF-TS exhibits a high HCOOH faradaic efficiency of $96 \pm 0.64\%$ at 400 mA cm^{-2} in acidic electrolyte and a high single-pass carbon conversion efficiency (SPCE) of 62.0%. Additionally, a Zn-CO$_2$ battery with Bi-MOF-TS as the cathode demonstrates a peak power density of 21.4 mW cm^{-2} and maintains stability over 300 cycles.

The environmental problems caused by the long-term reliance on fossil fuels and the large amount of CO$_2$ emissions have received global attention[1–6]. Electrochemical reduction of CO$_2$ (CO$_2$RR) to value-added fuel using electricity generated from intermittent energy sources such as solar and wind energy is a promising solution to mitigate greenhouse gas emissions[7–9]. Currently, among various CO$_2$ reduction products like carbon monoxide (CO)[10–12], methane (CH$_4$)[13–15], formic acid (HCOOH)[16–20], ethylene (C$_2$H$_4$)[21–23], and ethanol (C$_2$H$_5$OH)[24], formic acid (HCOOH)/formate (HCOO$^-$) stands out as a particularly promising option for commercialization. This is due to HCOOH being regarded as a promising reactant in fuel cells and as renewable hydrogen carrier molecules, owing to its high storage density. Additionally, HCOOH/HCOO$^-$ serve as raw materials in various industries, including silage preservation, as additives in animal feeds, for textile finishing, as anti-icing agents, and as intermediates in the chemical and pharmaceutical industries[25,26]. Bi-based catalysts are regarded as the most promising CO$_2$RR catalysts with high HCOO$^-$ selection because of their low toxicity, low price, and suitable binding capacity to *OCHO[27,28].

[1]State Key Laboratory of Advanced Technology for Materials Synthesis and Processing, Wuhan University of Technology, Wuhan, Hubei, PR China. [2]School of Chemical Sciences, University of Auckland, Auckland, New Zealand. [3]School of Materials and Energy, University of Electronic Science and Technology of China, Chengdu, PR China. [4]School of the Environment and Safety Engineering, Jiangsu University, Zhenjiang, PR China. [5]Nanotechnology Centre, Centre for Energy and Environmental Technologies (CEET), VŠB—Technical University of Ostrava, Ostrava-Poruba, Czech Republic. [6]SEU-FEI Nano-Pico Center, Key Laboratory of MEMS of the Ministry of Education, The Southeast University, Nanjing 210096, PR China. [7]These authors contributed equally: Xingbao Chen, Ruihu Lu, Chengbo Li. ✉e-mail: luowen_1991@whut.edu.cn; jxzhu@whut.edu.cn; ziyun.wang@auckland.ac.nz; mlq518@whut.edu.cn

Generally, during the CO_2RR process, a negative reduction potential leads to universal valence reduction behavior accompanied by reconstruction of Bi-based precatalysts[29,30]. Numerous defect sites formed in the reconstruction process, demonstrating better activity compared to inert integral sites[31]. Besides, introducing heteroatom doping and crystal lattice dislocations can also create high active sites[9,17,22]. However, those strategies only raise the activity at those particular sites, and massive pure Bi sites remain relatively low activity. Although industrial-level partial current density can be achieved in alkaline systems, CO_2 tends to react with alkaline electrolytes leading to a low CO_2 conversion efficiency. Using acidic electrolytes can effectively avoid the loss of CO_2, indicating greater potential for industrial applications. However, due to the limited number of high active sites, achieving industrial-level partial current density of formic acid in acidic systems remains a challenge. Recently, Liu et al. reported a BiOCl catalyst which exhibited 91% FE_{HCOOH} at -1.6 V vs. Ag/AgCl, with a current density of about -20 mA cm^{-2} (pH = 2)[32]. Marc et al. achieved FE_{HCOOH} of 77.1% at a current density of -100 mA cm^{-2} (pH = 1)[33]. These researches indicated that in acidic electrolytes, serious hydrogen evolution reaction (HER) is a tough issue with high proton concentrations, especially at high current density. Moreover, the coordinatively unsaturated defect sites can absorb oxygenated species from electrolytes, potentially poisoning the sites and diminishing the catalysts' selectivity and stability[25]. Therefore, activating the inert sites on Bi presents a promising approach to achieving high current density and high FE_{HCOOH} in acidic electrolytes. It is noteworthy that lattice strain may arise around defect sites, either as a response to minimize surface energy or due to lattice distortion[31]. The lattice strain effect typically diminishes from the defect or interface sites towards the periphery, thereby influencing the electronic structure of numerous sites[34]. This presents a potential avenue for activating as many sites as possible. Generally, the lattice strain can be induced by applying and controlling an external force on electrocatalysts, such as ion bombardment[35], substrate bending[36], thermal deforming[37], and ion intercalating/extracting[38]. However, the impact of these methods on the structural perturbation of Bi-based pre-catalysts and their subsequent reconstruction after CO_2RR remains largely unexplored.

Herein, we introduce large-area tensile strain in the catalyst by guiding catalyst reconstruction to fabricate continuous vacancies, thereby activating more inert sites. Density functional theory (DFT) calculations indicate that continuous vacancies induce higher and broader tensile strain on peripheral Bi sites, enhancing the adsorption of *OCHO intermediate and activating more distant sites than single vacancies. We regulated the reconstruction process of Bi-MOF by applying two different external forces-mechanical force (Bi-MOF-MF) and thermal shock (Bi-MOF-TS), respectively, to modify the structure of pre-catalysts. In-situ X-ray absorption fine structure (XAFS) and in-situ Raman spectra revealed that tiny Bi clusters were formed in Bi-MOF-TS, and both Bi-MOF-MF and Bi-MOF-TS underwent a more drastic reconstruction process during CO_2RR due to the weaker Bi–O bonding strength. High-angle annular dark-field scanning transmission electron microscopy (HAADF-STEM) images and strain simulations revealed that post-reconstructed Bi^0 nanosheets from Bi-MOF-MF and Bi-MOF-TS contained more Bi vacancies which generated significant tensile strain on adjacent non-defective Bi sites. More Bi vacancies were created on the Bi^0 derived from Bi-MOF-TS because of the deposition of Bi^0 units on tiny Bi clusters, which resulted in a larger area of peripheral Bi sites experiencing stronger tensile strain. Consequently, this strategy resulted in a faradaic efficiency (FE) exceeding 90% over a broad potential range of 800 mV and at the industrial ampere-level current density. Moreover, it enabled a FE of $96 \pm 0.64\%$ for formic acid production at 400 mA cm^{-2} in an acidic electrolyte (pH = 1.5 ± 0.2). Industrial-oriented Zn-CO_2 batteries and all-solid-electrolyte reactor tests further proved the practicability and stability of the prepared catalyst.

## Results
DFT calculations

To enhance the understanding of CO_2RR activity on Bi sites, we employed first-principles calculations to examine the impact of vacancies. Initially, we modeled various Bi slabs, including pure Bi, Bi-1SV, Bi-2SV, and Bi-3SV, to simulate the accumulation of SVs (Supplementary Fig. 1). The bond length of Bi atoms near SVs elongated along the direction of SV, with the degree of stretching being highly dependent on the distance from the SVs (refer to Table S1). This confirms that the incorporation of SVs introduces a uniaxial strain on the neighboring Bi sites (Fig. 1a). Subsequently, we calculated the energy profiles of the CO_2RR towards HCOOH on a possible Bi site on Bi-1SV (Fig. 1b). Pure Bi, with weak adsorption behavior, displays negligible CO_2RR activity, whereas the strong adsorption of Bi-1SV enables the activation of CO_2 and high CO_2RR activity. In addition, the CO_2RR activity of adjacent Bi sites was found to depend on the relative site distance relative to the SVs, with Bi sites in closer proximity to the SVs exhibiting better activity.

In reconstructed catalysts, continuous vacancies or grain boundaries are typically present. To investigate the role of the build-up SVs in CO_2RR activities, the free energy change of CO_2RR on Bi-2SV and Bi-3SV was also calculated (Supplementary Figs. 2 and 3). On SV sites (site 1), higher SV concentrations rise leading to lower overpotential and better CO_2RR performance (Fig. 1c). Increasing SVs in the same orientation promotes the activity of more Bi sites (such as sites 2–4) in the vicinity of SVs.

Furthermore, the underlying mechanism of build-up SVs was further studied. As discussed in our previous work[39], a more positive p-band center endows pure Bi with weak adsorption, making it difficult to activate CO_2. In contrast, SV sites exhibit strong adsorption due to their lower p-band center, enabling CO_2RR to be limited to the release of HCOOH (Fig. 1d). As we observed (Fig. 1e), the strain on Bi sites promotes the adsorption of *OCHO intermediates, accelerating the CO_2RR, which is consistent with previous findings. Furthermore, increased strain can enhance the adsorption of *OCHO, and a higher density of vacancies can introduce greater strain to the surrounding sites (Table S1). In the continuous vacancy model (Bi-3SV), ~3% stress can lead to an almost optimal *OCHO adsorption capacity. Therefore, the SV buildups can concurrently promote both SV sites and large-area adjacent Bi sites by tuning the p-band center and inducing strain, respectively, resulting in a enhancement of CO_2RR activities.

Materials synthesis and characterization

Generally, the reduction of Bi$^{\delta+}$ involves the radical restructuring of Bi units, making it difficult to uncover the relationships between structures and performances in the presence of a large number of Bi sites. We choose MOF as the research model to study the induction effect of structural perturbation of the pre-catalyst on the reconstruction behavior, because it has the characteristics of isolated Bi sites. Atomically dispersed Bi sites can be reduced to smaller nanosheets/nanoparticles than those in Bi-based oxides, potentially exposing more active sites−both high-activity and low-activity−and inducing greater surface strain on the Bi. Additionally, the limited number of sites facilitates studying the effect of increasing the proportion of highly active sites on overall performance. Bi-MOF nanosheets (Supplementary Fig. 4) were prepared based on earlier reports[40]. To investigate the impact of the structure of pre-catalysts on electrochemical reconstruction process, the Bi-MOF was treated with violent mechanical ball milling and mild instantaneous Joule thermal shock. Compared to Bi-MOF, Bi-MOF-MF nanosheets that were treated with ball milling showed a fragmented structure (Supplementary Fig. 5). In addition, the morphology of Bi-MOF-TS nanosheets treated with Joule heating did not significantly change (Supplementary Fig. 6), indicating that fast thermal shock had a negligible effect on the micromorphology. HAADF-STEM images and energy dispersive X-ray spectroscopy (EDX)
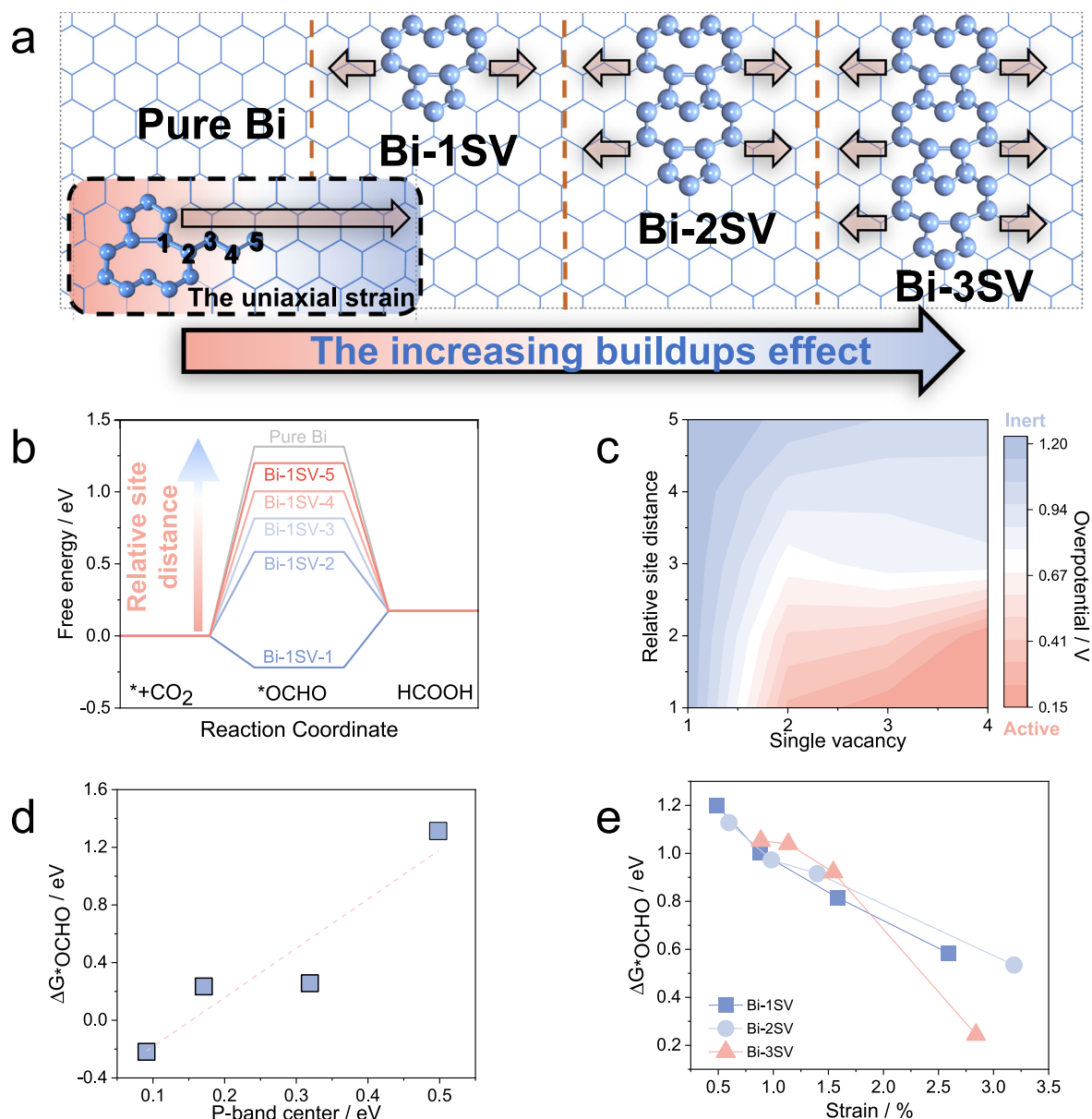
Fig. 1 | DFT calculations. Theoretical simulations **a** Schematic illustration of the increasing buildup effect as a single vacancy (SV) assembles. The lines and spheres represent planar Bi and Bi near SVs. The arrows denote the uniaxial strain. The inset highlights possible sites under uniaxial strain, and the number is labeled as possible sites along the uniaxial strain direction. **b** Free energy profile of CO_2RR towards HCOOH on various Bi sites. **c** Color contour plot of CO_2RR activity (Overpotential) as a function of SV number and relative site distance to SVs. **d** Correlation between ΔG_{*OCHO} and the p-band center of SV Bi sites. **e** ΔG_{*OCHO} versus uniaxial strain of Bi sites close to SVs. Source data for Fig. 1b–e are provided as a Source Data file.

mapping show that the elemental composition of the three pre-catalysts is still evenly distributed, and there is no obviously formation of Bi particles (Supplementary Figs. 7–9). As shown in Fig. 2a, X-ray diffraction (XRD) patterns confirm that after mechanical force treatment, the crystallinity degree of Bi-MOF-MF is obvious lower than that of Bi-MOF. Unexpectedly, after thermal shock, Bi-MOF-TS is in an amorphous state instead of maintaining its crystal characteristics, indicating that the Bi-MOF-TS nanosheets went through a more radical structural alternation. However, the Fourier transform infrared (FT-IR) spectra (Fig. 2b) of the three pre-catalysts show no holistic structural destruction, and the ligands of Bi-MOF still exist. It is noteworthy that in the FT-IR spectra, the relative strength of Bi–O bonds to C=C bonds in the aromatic ring significantly decreased in Bi-MOF-MF, meaning that Bi–O bonds were partially broken in Bi-MOF-MF due to mechanical force without changing the overall structure of the MOF. The X-ray absorption near-edge structure (XANES) spectra of the Bi L_3-edge

(Supplementary Fig. 10) revealed that the valence states of Bi in Bi-MOF-MF and Bi-MOF-TS were reduced compared to pristine Bi-MOF, further demonstrating the partial breakage of Bi–O bonds. As shown in Supplementary Figs. 11 and 12 the percentage of Bi^0 in Bi-MOF-MF and Bi-MOF-TS are 33% and 45% respectively, indicating that Bi^{3+} sites can undergo partial conversion into Bi^0 under mechanical and thermal forces. Then, the coordination structure was ascertained by Fourier transform extended X-ray absorption fine structure (FT-EXAFS) spectroscopy. The length of the Bi–O bonds in Bi-MOF-MF (2.18 Å) and Bi-MOF-TS (2.23 Å) are significantly elongated compared to Bi-MOF, with the elongation in Bi-MOF-TS being more pronounced than in Bi-MOF-MF (Fig. 2c and Supplementary Figs. 13–15). In addition, two weak peaks corresponding to the Bi–Bi bond and one strong peak corresponding to Bi–O–Bi coordination can be found in Bi-MOF-TS, indicating the formation of fine Bi clusters. The Bi–O coordination number of Bi-MOF-MF and Bi-MOF-TS are 4.48 ± 0.53 and 3.2 ± 0.79,
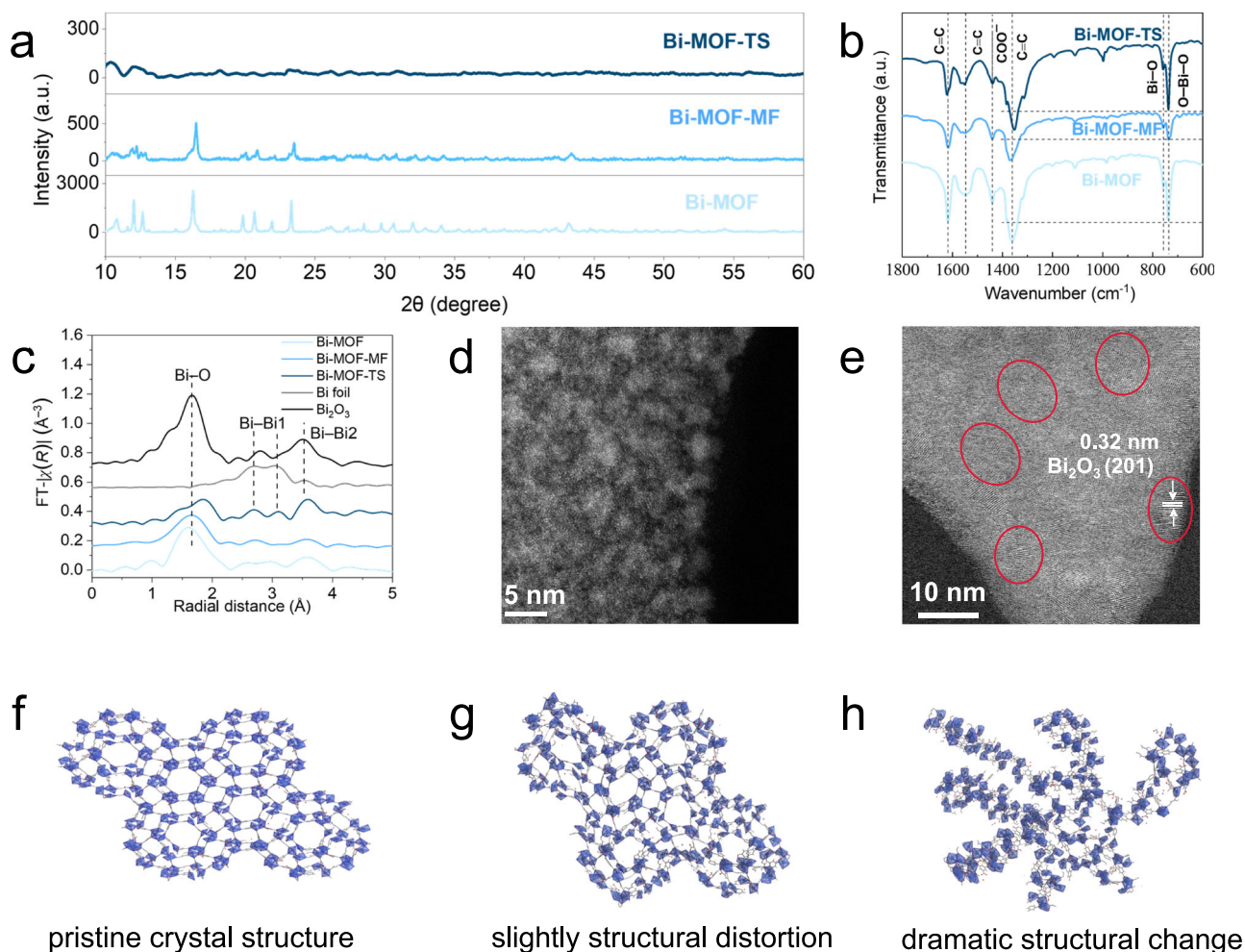
Fig. 2 | Materials characterization. a XRD pattern of Bi-MOF, Bi-MOF-MF, and Bi-MOF-TS. **b** FT-IR analysis of Bi-MOF, Bi-MOF-MF, and Bi-MOF-TS. **c** The Bi L_3-edge EXAFS spectra of Bi-MOF, Bi-MOF-MF, and Bi-MOF-TS. Bulk Bi foil and Bi_2O_3 are listed as references. HAADF-STEM image of Bi-MOF-MF (**d**) and Bi-MOF-TS (**e**). Schematic illustration of the crystal structure of Bi-MOF (**f**), Bi-MOF-MF (**g**), and Bi-MOF-TS (**h**). The structure models are proposed from based on the results of XRD, FT-EXAFS, and FT-IR. Source data for Fig. 2a, b, and c are provided as a Source Data file.

respectively (Table S2). Thus, the local coordination structures of Bi-MOF-MF and Bi-MOF-TS have been significantly changed, and the bonding strength between Bi and O is obviously weakened.

To visually observe the atomic distribution in the three types of catalysts, HAADF-STEM was used for intuitive characterization. As shown in Fig. 2d and Supplementary Fig. 16, the Bi sites in Bi-MOF and Bi-MOF-MF retained an atomic distribution. However, small clusters/particles were found in Bi-MOF-TS with a size of 1.6–2.6 nm (Supplementary Fig. 17), and the transmission electron microscopy (TEM) image of Bi-MOF-TS manifested exposure of the (201) facet of Bi_2O_3 (Fig. 2e). This might be because the Bi atoms yielded from the breaking of the Bi−O bond aggregated into scattered tiny clusters/particles during thermal shock, which were oxidized by oxygen in the air into Bi_2O_3. No Bi or Bi_2O_3 peaks were detected in the XRD spectra (Fig. 2a) for Bi-MOF-TS, demonstrating that the particles were scattered and tiny and were expected to be the original nucleation sites during electrochemical reconstruction. In summary, Bi-MOF-MF and Bi-MOF-TS both underwent disturbance of structure and coordination around Bi sites, with Bi-MOF-TS experiencing more dramatic changes (Fig. 2f−h).

CO₂ electro reduction performance
To evaluate the CO₂RR performance of Bi-MOF, Bi-MOF-MF, and Bi-MOF-TS, these catalysts were sprayed onto a gas diffusion electrode (GDE) and then assessed in a flow cell electrolyzer with 1 M KOH

electrolyte (Supplementary Fig. 18). The gas and liquid products were quantitatively analyzed by gas chromatography (GC) and ^1H nuclear magnetic resonance (NMR) spectroscopy, respectively. Formate was the only liquid product (Supplementary Fig. 19), and CO was the only C_1 product detected in the gas product (Supplementary Fig. 20). As shown in Fig. 3a, the FE of formate for Bi-MOF can reach 93.0 ± 0.7% at −0.9 V (vs. reversible hydrogen electrode (RHE), unless otherwise specified), but lower at other applied potentials. Bi-MOF-TS shows the optimal formate selectivity among the three catalysts and achieves over 90% formate FE in a potential range of 800 mV (from −0.6 V to −1.3 V), which is better than that of Bi-MOF-MF (600 mV) and other reported catalysts. With regard to Bi-MOF-MF and Bi-MOF-TS, the FE for CO and H_2 were lower than 5% throughout the entire potential range. In contrast, Bi-MOF exhibited a much higher FE for H_2 at a relatively more negative potential, reaching 47 ± 10.1% at −1.3 V. Linear sweep voltammetry (LSV) curves were in a flow cell at a scan rate of 10 mV s^{-1} (Supplementary Fig. 21). Compared with Bi-MOF, Bi-MOF-MF and Bi-MOF-TS showed significantly higher current densities, −945 mA cm^{-2} and −1301 mA cm^{-2} at −1.5 V, respectively. Thus, Bi-MOF-TS obtains a high partial current density for formate production (J_{HCOO^-}) of −995 mA cm^{-2} (Supplementary Fig. 22), much higher than that of Bi-MOF-MF (−642 mA cm^{-2}) and Bi-MOF (−169 mA cm^{-2}). Bi-MOF-TS outperformed the reported catalysts in terms of the FE of HCOO$^-$ and the highest partial current density of formate (Fig. 3b and
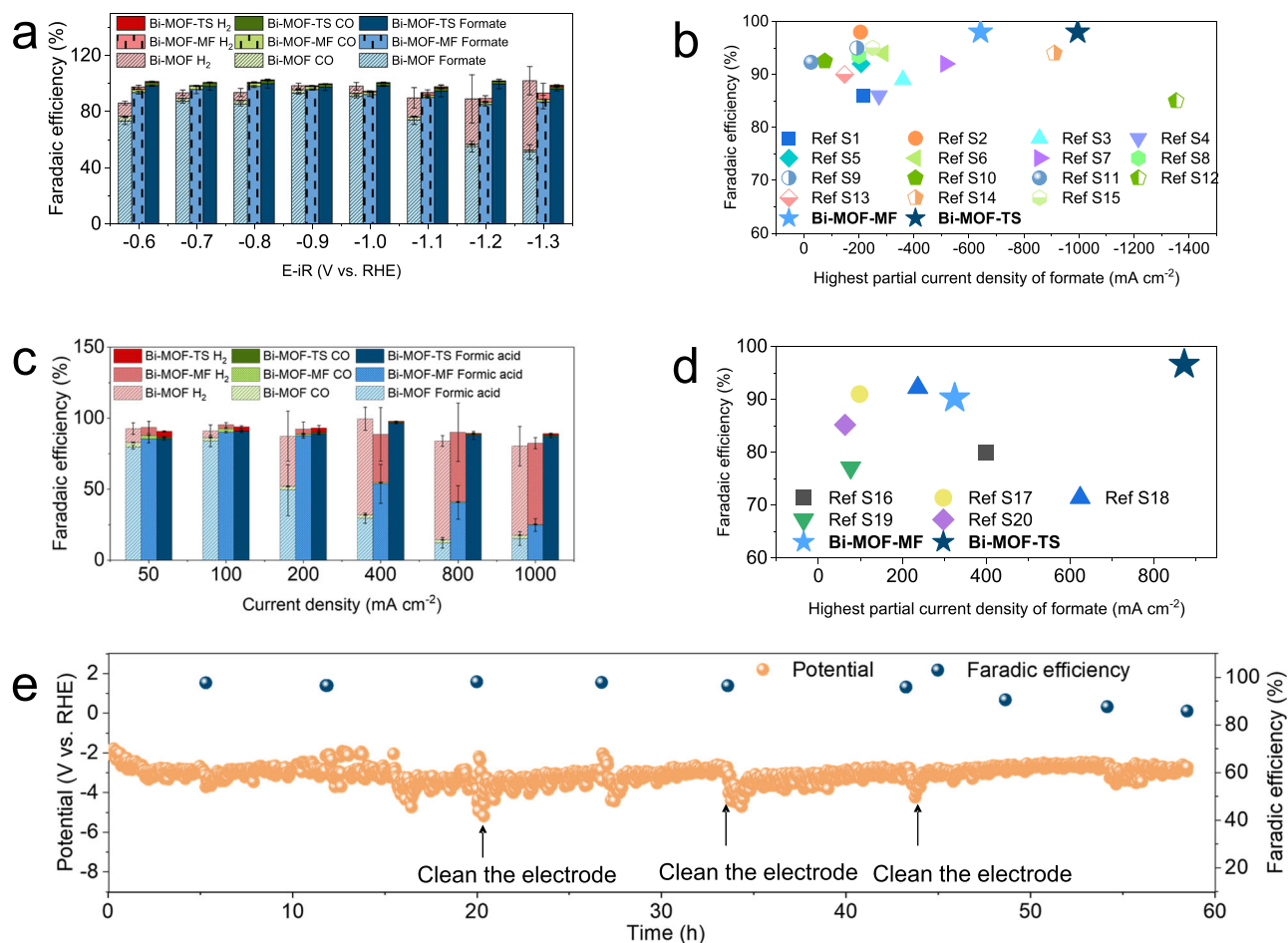
**Fig. 3 | CO₂ electroreduction performance. a** The FE of HCOO⁻ and H₂, CO for Bi-MOF, Bi-MOF-MF and Bi-MOF-TS in 1 M KOH (pH = 14 ± 0.1). We applied 3 Ω (75%) IR correction for the test. **b** Comparison of FE of HCOO⁻ and highest partial current density of formate for Bi-MOF-MF, Bi-MOF-TS, and recently reported Bi-based catalysts in alkaline system. **c** The FE of HCOOH, CO and H₂ for Bi-MOF, Bi-MOF-MF, Bi-MOF-TS in acidic electrolyte. IR correction was not applied. **d** Comparison of HCOOH FE and highest partial current density for HCOOH for the three catalysts in acidic electrolyte. **e** stability test for Bi-MOF-TS in a flow-cell at current density of 500 mA cm⁻² in acidic electrolyte (pH = 1.5 ± 0.2). No IR correction was performed. All tests were performed at room temperature. Source data for Fig. 3a–e are provided as a Source Data file.

Table S3). Furthermore, Bi-MOF-TS exhibited a formate FE of over 90% across a potential range of 800 mV (from −0.6 V to −1.3 V), which is broader than that of other catalysts reported (Supplementary Fig. 23). High formate selectivity over a wider voltage range can only be achieved with further antitoxic chemical protection of the active site. To investigated the inhibitory effects of three catalysts on HER, we conducted LSV tests on them in the absence of CO₂. The result showed that the hydrogen evolution activity of Bi-MOF-TS is significantly lower than that of Bi-MOF and Bi-MOF-MF (Supplementary Fig. 24).

Due to the inhibition of HER in alkaline electrolytes, it may not be necessary to have a large number of highly active sites, and thus the Bi-MOF-TS didn't show significant advantage in current density and formate selectivity compared to Bi-MOF-MF. In addition, the formation of carbonates occurs in alkaline electrolytes, reducing single-pass CO₂ conversion efficiency and obstructing the GDE. This effect considerably raises the energy and economic costs and affects the stability of the system. Using acidic electrolytes significantly enhances carbon efficiency and operational stability, as CO₂ remains non-reactive in acidic environments. However, in acidic electrolytes, the high H⁺ coverage on non-defective inert sites may result in intense HER competitive reaction. Therefore, we performed CO₂RR for three catalysts in both neutral and acidic (pH = 1.5 ± 0.2) electrolytes. According to Fig. 3c, across the entire range of current densities, Bi-MOF-TS demonstrated the lowest hydrogen evolution activity in acidic

electrolyte. Moreover, it exhibited a high FE for HCOOH production (96 ± 0.64% at 400 mA cm⁻², FE_{H2} = 0.63 ± 0.13%, FE_{CO} = 0.65 ± 0.47%), maintaining considerable efficiency even at 1000 mA cm⁻² (87 ± 0.92%, FE_{H2} = 0.91 ± 0.50%, FE_{CO} = 0.84 ± 0.16%). In contrast, both Bi-MOF and Bi-MOF-MF showed higher hydrogen evolution activity at elevated current densities. Furthermore, Bi-MOF-TS achieved the highest partial current density for HCOOH production when compared with Bi-MOF and Bi-MOF-MF (Supplementary Fig. 25). The performance of Bi-MOF-TS in acidic electrolytes far surpassed that of Bi-based catalysts reported to date (Fig. 3d and Table S4). Compared to other materials reported in acidic electrolytes, Bi-MOF-TS exhibits higher FE and partial current density for formic acid. Despite the hydrogenation of intermediate does lead to the increase of the local pH due to the consumption of H⁺. At low and moderate current densities (−500 mA cm⁻²), the electrode surface remains acidic or neutral. Even at high current densities (−1000 mA cm⁻²) the surface environment just exhibits slight alkalinity, and which rapidly reverts to acidic with increasing distance from the electrode surface[41]. Considering only the electrode surface, Bi-MOF and Bi-MOF-MF still show high FE for H₂ because of the limited number of active sites, according to the performances in alkaline and neutral electrolytes (Fig. 3a and Supplementary Fig. 27). While Bi-MOF-TS exhibits good performances in alkaline, neutral, and acidic electrolytes, attributed to the activation of inert sites on Bi.
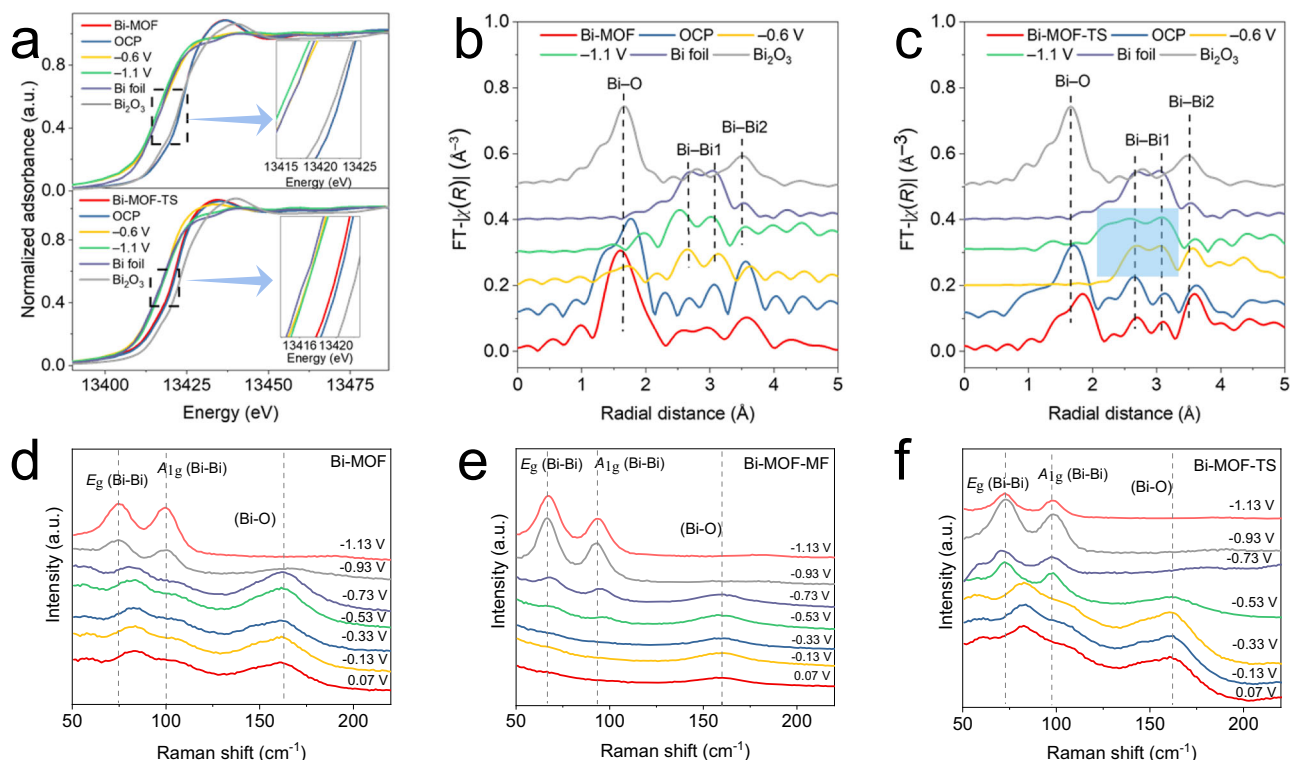
Fig. 4 | In-situ XAS and Raman spectra characterization. a In-situ Bi L_3-edge XANES spectra of Bi-MOF and Bi-MOF-TS under different applied potentials. Bulk Bi foil and Bi_2O_3 are listed as references. The inserts are localized magnification of the highlighted sections. In-situ Bi L_3-edge EXAFS spectra of Bi-MOF (**b**) and Bi-MOF-TS (**c**) under different applied potentials. In-situ Raman spectra of Bi-MOF (**d**), Bi-MOF-MF (**e**), and Bi-MOF-TS (**f**) at different applied potentials (reference to RHE). Source data for Fig. 4a–f are provided as a Source Data file.

We assessed the single-pass CO_2 conversion efficiency (SPCE) of the three catalysts by adjusting the CO_2 flow rate. We conducted tests under the flow rate of CO_2 from 50 to 1 standard cubic centimeters per minute (sccm). The SPCE of Bi-MOF-TS increased from 1.8% at 50 sccm to 62.0% at 1 sccm, significantly higher than that of Bi-MOF (8.6%) and Bi-MOF-MF (30.5%) (Supplementary Fig. 26). The CO_2RR performance in neutral environment also present the superiority of Bi-MOF-TS, indicating the HER inhibition in OH^--deficient environment requires more highly active sites (Supplementary Figs. 27 and 28). To demonstrate the stability of Bi-MOF-TS at industrial current density in acidic electrolyte (pH = 1.5 ± 0.2), Bi-MOF-TS showed stable CO_2RR performance at $500\,mA\,cm^{-2}$ with 85% FE of HCOOH after 60 h test (Fig. 3e).

The electrochemical active surface area (ECSA) test performed on the catalysts after CO_2RR at −1.1 V for 3 h showed that Bi-MOF-MF-derived Bi^0 nanosheets exhibited an apparent increase in the active area (Supplementary Figs. 29 and 30), which could be attributed to the increase in the surface area of Bi-MOF-MF during the mechanically induced process. The active surface areas of Bi^0 nanosheets derived from Bi-MOF and Bi-MOF-TS were relatively similar. Therefore, we believe that the active surface area is not a determining factor of CO_2RR performance in our work, but the intrinsic activity of the active sites is.

Mechanistic understanding

To investigate how the coordination structure of pre-catalysts influences the electrochemical reconstruction process and to understand the relationship between structure and performance, we employed in-situ X-ray absorption spectroscopy (XAS) at a Synchrotron Radiation Source (Supplementary Fig. 31). The XANES spectra of the Bi L_3-edge reveal that the Bi in Bi-MOF and Bi-MOF-TS shows a complete valence reduction from Bi^{3+} to Bi^0 under CO_2RR conditions (Fig. 4a)[42]. FT-EXAFS spectra show the variation in the coordination structure for Bi sites (Fig. 4b, c). It is remarkable that Bi-MOF exhibits a distinct Bi−O signal at −0.6 V[43], demonstrating that Bi^{3+} was not completely reduced

to Bi^0. However, for Bi-MOF-TS, Bi−O coordination completely disappeared at −0.6 V. We believe the partial reduction of Bi sites in Bi-MOF-TS pre-catalysts is responsible for this. When the applied potential shifted to −1.1 V, both Bi-MOF and Bi-MOF-TS were reconstructed to Bi^0. A subtle difference is that Bi-MOF-derived Bi displays a regular coordination structure similar to Bi foil, while Bi-MOF-TS-derived Bi exhibits a more disordered coordination structure that may construct more defect sites. In Bi-MOF, discrete Bi^{3+} sites were slowly reduced and sluggishly reorganized into a completed lattice, and therefore, fewer structural and coordination defects were formed. In contrast, tiny Bi particles in Bi-MOF-TS may serve as original nucleation sites during the reconstruction process, and other separated Bi units would continue to grow along the Bi particles. Due to the rapid reconstruction, different crystal nuclei might not fuse well, resulting in a chaotic Bi−Bi coordination structure (the blue zone in Fig. 4c). K-space figures for in-situ XAS were plotted in Supplementary Figs. 32 and 33.

In situ Raman spectroscopy is also an important characterization method for observing the variation in the coordination environment of catalysts under different reaction potentials[44–46]. The Bi−Bi coordination signals at ~75 cm^{-1} and 100 cm^{-1} for Bi-MOF appeared at −0.93 V[43,47], indicating that Bi-MOF was reconstructed at a relatively negative potential and underwent a sluggish reconstruction process (Fig. 4d). In contrast, Bi-MOF-MF and Bi-MOF-TS showed Bi^0 signals at −0.73 V and −0.53 V, respectively (Fig. 4e, f). No Bi^0 was detected for Bi-MOF-TS in the initial state, which may be ascribed to the tiny Bi clusters feature. These results further confirm the fast reconstruction process of Bi-MOF-TS leading to a more drastic rearrangement of Bi atoms.

We characterized the three catalysts after CO_2RR to determine the structure of derived Bi^0. XRD patterns of the three catalysts after the CO_2RR also confirmed that Bi^{3+} in the precatalysts was reduced to Bi^0 (Supplementary Fig. 34). From the XRD, we found that (012) facet was dominant in three pre-catalysts-derived Bi^0. The outcome illustrated that exposed facet is not the reason affecting the selectivity and
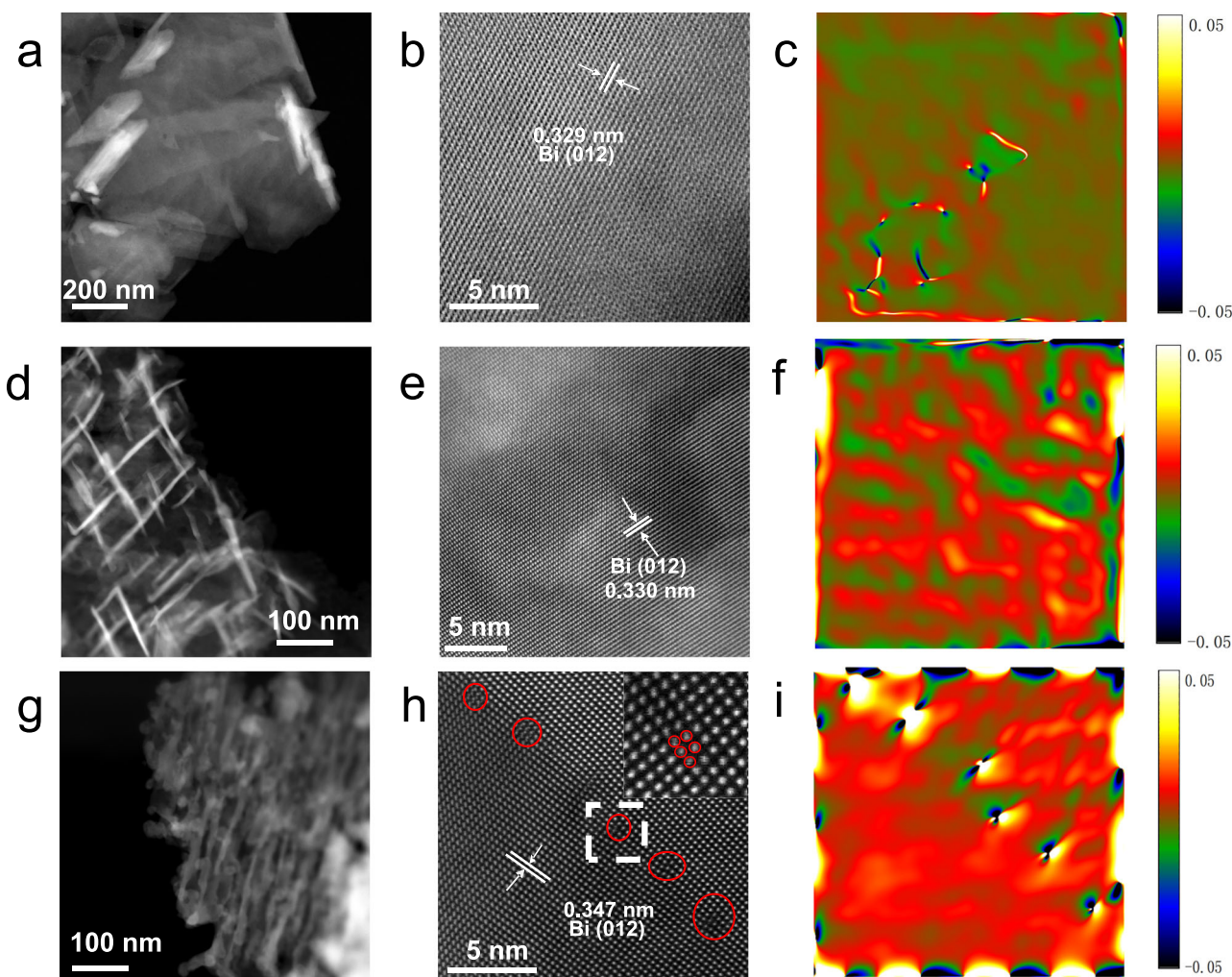
Fig. 5 | Structural characterization of catalysts after the CO₂RR. a, b HAADF-STEM image of the Bi-MOF-derived Bi nanosheets. **d, e** HAADF-STEM image of Bi-MOF-MF-derived Bi nanosheets **g, h** HAADF-STEM image of Bi-MOF-TS-derived Bi. The insert in Fig. 5h is the magnification of the white-framed section. **c, f, i** Strain simulation of Bi-MOF-derived Bi nanosheets, Bi-MOF-MF-derived Bi nanosheets, and Bi-MOF-TS-derived Bi nanosheets. The colorful bars in (**c, f, i**) represent the intensity of strain, where positive values indicate tensile strain and negative values indicate compressive strain.

activity. It should be noted that the (012) facet diffraction peak of Bi-MOF-TS-derived Bi^0 and Bi-MOF-MF-derived Bi^0 shift to smaller angle compared to that of Bi-MOF-derived Bi^0, with a more pronounced shift observed on the former. The phenomenon indicated that the presence of tensile strain in Bi-MOF-TS-derived Bi^0 and Bi-MOF-MF-derived Bi^0, with the strain being more significant in the Bi-MOF-TS-derived Bi^0. Specifically, the tensile strain measured on the 012 facet of Bi-MOF-MF was 0.30%, whereas it was 2.84% for Bi-MOF-TS. To uncover the reconstructed microstructure of Bi^0 derived from the three pre-catalysts and determine the true active sites, we implemented HAADF-STEM and the corresponding strain simulation for post-catalysts. The samples of derived-Bi^0 nanosheets were collected by dropping the ink of catalysts onto indium tin oxide-coated glass and electrolyzing at −1.1 V for 3 h in CO_2-saturated 0.5 M $KHCO_3$. As shown in Fig. 5a, d, Bi-MOF and Bi-MOF-MF reconstructed into stacked smooth nanosheets at negative potential. The Bi-MOF-TS-derived Bi^0 nanosheets showed a nanosheet structure composed of nanoparticles (Fig. 5g), which were formed from the preformed Bi crystal nucleus (as mentioned earlier, formed during thermal induction in Bi-MOF-TS). The size of Bi particles primarily ranges from 14 nm to 26 nm. (Supplementary Fig. 35). In addition, EDX mapping also showed the uniform distribution of Bi, O, and C in the three derived Bi^0 nanosheets in nanoparticles formed from preformed Bi crystal nucleus in Bi-MOF-TS-derived Bi^0

(Supplementary Figs. 36–38). The O was present because Bi was partially oxidized in the air, and C originated from the metal organic framework. The (012) facet of Bi-MOF-derived Bi^0 illustrated an interplanar spacing of 0.329 nm (Fig. 5b), and weak strain (<1%) was observed on the complete crystal plane (Fig. 5c). In addition, the distance between atoms can intuitively reveal the existence of strain[34,48–50]. To simulate the strain from the interlayer of (012) phase for Bi-MOF-derived Bi^0, we measured the interlayer distance at two different positions, which were 0.332 nm and 0.329 nm, respectively, indicating that a weak strain may exist on the crystal plane (Supplementary Fig. 39). The Bi-MOF-MF-derived Bi^0 nanosheets exposed the (012) facet with 0.330 nm interplanar spacing (Fig. 5e). According to the strain simulation diagram, a significant tensile strain was present in most crystal planes (Fig. 5f). The atomic distance at the 2nd position was 0.344 nm, and that at for the 1st position was 0.330 nm (Supplementary Fig. 40). The distance in another position was measured (0.328 nm) to determine the strain distribution (Supplementary Fig. 41). Those results demonstrated that tensile strain exists locally in Bi-MOF-MF-derived Bi^0 nanosheets. As seen from Fig. 5h, continuous vacancies (SV defects) arranged like a line, possibly due to the imperfect fusion between two crystal nuclei during the drastic reconstruction process. A higher tensile strain density was observed on the crystal plane near the SV-defects (Fig. 5i), indicating that SV-defects,
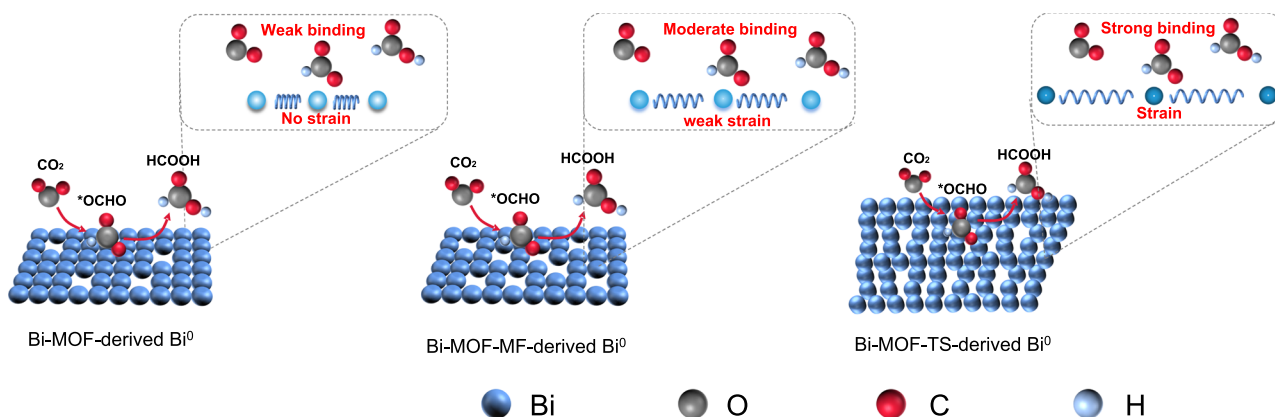
Fig. 6 | Schematic illustration. Comparison of the structure of post-reconstructed Bi^0 nanosheets, and the binding capacity to *OCHO on Bi^0 nanosheets with different strains.

unlike other reported point defects which only themselves were active sites, could also have an impact on their surroundings. Within the same distance, six atoms were on the side with an average atom distance of 0.309 nm, but only five atoms were on the side with tensile strain corresponding to a distance of 0.361 nm (Supplementary Fig. 42). In addition, the atom distance at other positions on the crystal plane was 0.347 nm (Supplementary Fig. 43), which was longer than that in the case without strain (0.330 nm).

These findings indicate that alterations in the coordination structure of Bi atoms within Bi-MOF can influence their reconstruction process, thereby affecting the microstructure of the derived Bi^0, as illustrated in Fig. 6. Supported by in-situ XAS, in-situ Raman spectroscopy, and HAADF-STEM analyses, we deduce that a faster reconstruction process results in a more significant rearrangement of Bi atoms. Additionally, due to the presence of original nucleation sites in Bi-MOF-TS, we were able to introduce continuous vacancies at the junction points of different crystal nuclei. This introduction led to more pronounced tensile strain compared to dispersed vacancies, which is the key reason to the superior CO_2 reduction reaction (CO_2RR) performance of Bi-MOF-TS across a broad pH range.

In-situ attenuated total reflection (ATR)-SEIRAS proves to be the optimal method for monitoring the surface coordination environment of electrodes[51,52]. As shown in Supplementary Fig. 44, all three catalysts illustrated two upwards improvement peaks at ~1400 cm^{-1} and ~1600–1620 cm^{-1} during CO_2RR, which were attributed to the symmetric and asymmetric stretching modes of COOH radicals (monodentate ligand configuration), respectively[53,54]. Therefore, the three catalysts showed high formate selectivity. In addition, the peak at around 1700–1730 cm^{-1} was assigned to the C=O stretching vibration of carboxylic acid, proving the production of formate. To comprehend the reaction kinetics and reaction mechanism of the CO_2RR on the three certain catalysts, Tafel slopes were plotted in Supplementary Fig. 45. The Tafel slope of Bi-MOF was observed to be 266 mV dec^{-1}, a value close to 200 mV dec^{-1}, suggesting a significant barrier for the adsorption of CO_2 onto active sites[55,56]. For Bi-MOF-MF and Bi-MOF-TS, lower Tafel slopes of 161 mV dec^{-1} and 154 mV dec^{-1}, respectively, were exhibited than those of Bi-MOF. This value is approaching to 118 mV dec^{-1} which is the theoretical value, indicating that the chemical rate-determining step is the first electron transfer step, namely, forming *CO_2^{-} [57]. Furthermore, the Tafel slope of Bi-MOF-TS was lower than that of Bi-MOF-MF, suggesting favorable kinetic activity for the reduction of CO_2 to formate over Bi-MOF-TS.

Practical demonstration
The Zn-CO_2 battery is considered a promising device to address environmental and energy issues simultaneously because it can reduce CO_2 to chemicals and fuel along with storing and outputting electricity[58–61]. We assembled Zn-CO_2 batteries with Bi-MOF, Bi-MOF-MF and Bi-MOF-TS cathodes for CO_2 to $HCOO^-$ conversion (Fig. 7a). The reaction that occurred at the cathode during discharging was the CO_2RR, while at the anode, it involved the conversion of zinc metal to $Zn(OH)_4^{2-}$, which could be certified by cyclic voltammetry (CV) (Supplementary Fig. 46). Regarding the charge process, the cathodic reaction was an oxygen evolution reaction, and $Zn(OH)_4^{2-}$ was reduced to Zn at the anode[62]. The discharge and charge polarization curves for the three catalysts were collected, showing that Bi-MOF-TS exhibited the highest discharge current density and Bi-MOF and Bi-MOF-MF demonstrated a relatively lower discharge current density (Fig. 7b). The higher discharge current density of Bi-MOF-TS is attributed to the more active sites and higher CO_2RR activity in 1 M $KHCO_3$ electrolyte. The charge current density of the three catalysts exhibited no significant difference. As shown in Fig. 7c, Bi-MOF-TS achieved a maximal power density of 21.4 mW cm^{-2} at 23.8 mA cm^{-2}, the highest value reported thus far. The peak power densities of other reported Zn-CO_2 batteries, where formate serves as the primary reduction product, are all below 10 mW cm^{-2} (Table S5). The maximal power densities of Bi-MOF and Bi-MOF-MF were lower than 5 mW cm^{-2}. Then, the Zn-CO_2 battery with the Bi-MOF-TS cathode was recycled at 2 mA cm^{-2} and each charge/discharge process were 5 min, namely, the charge/discharge capacity of Zn-CO_2 battery was fixed at 1/6 mA h cm^{-2} (Fig. 7d). The assembled Zn-CO_2 battery also showed favorable rechargeability and stable operation for 300 cycles (up to 50 h), illustrating a 2.11 V voltage gap.

As is well known, due to the flooding problem, the assessment of catalyst stability in flow cells is frequently prone to inaccuracies[63–65]. Using an all-solid electrolyte cell, CO_2 can be converted into pure formic acid without complex steps for product separation and purification, and the catalysts are not affected by flooding[66,67]. Deionized water was used to slowly rinse the solid electrolyte region, resulting in the collection of pure formic acid. Bi-MOF-TS showed a considerable formic acid FE at current densities from −50 mA cm^{-2} to −200 mA cm^{-2} (Supplementary Fig. 47). The relationship between energy efficiency and current density indicates that Bi-MOF-TS achieves the highest energy efficiency of 33.5% at 50 mA cm^{-2} (Supplementary Fig. 48). Furthermore, Bi-MOF-TS showed good stability at 50 mA cm^{-2} (which was 200 mA cell current) for 24 h (Fig. 7e).

Discussion
In summary, we have uncovered the positive impact of uniaxial tensile strain introduced by Bi vacancies on the CO_2RR performances of non-defective Bi sites. Through the application of mechanical forces and thermal shock treatment, we synthesized two pre-catalysts, namely, Bi-MOF-MF and Bi-MOF-TS. These catalysts exhibit a weaker Bi–O coordination strength, with some Bi units forming as small clusters within Bi-
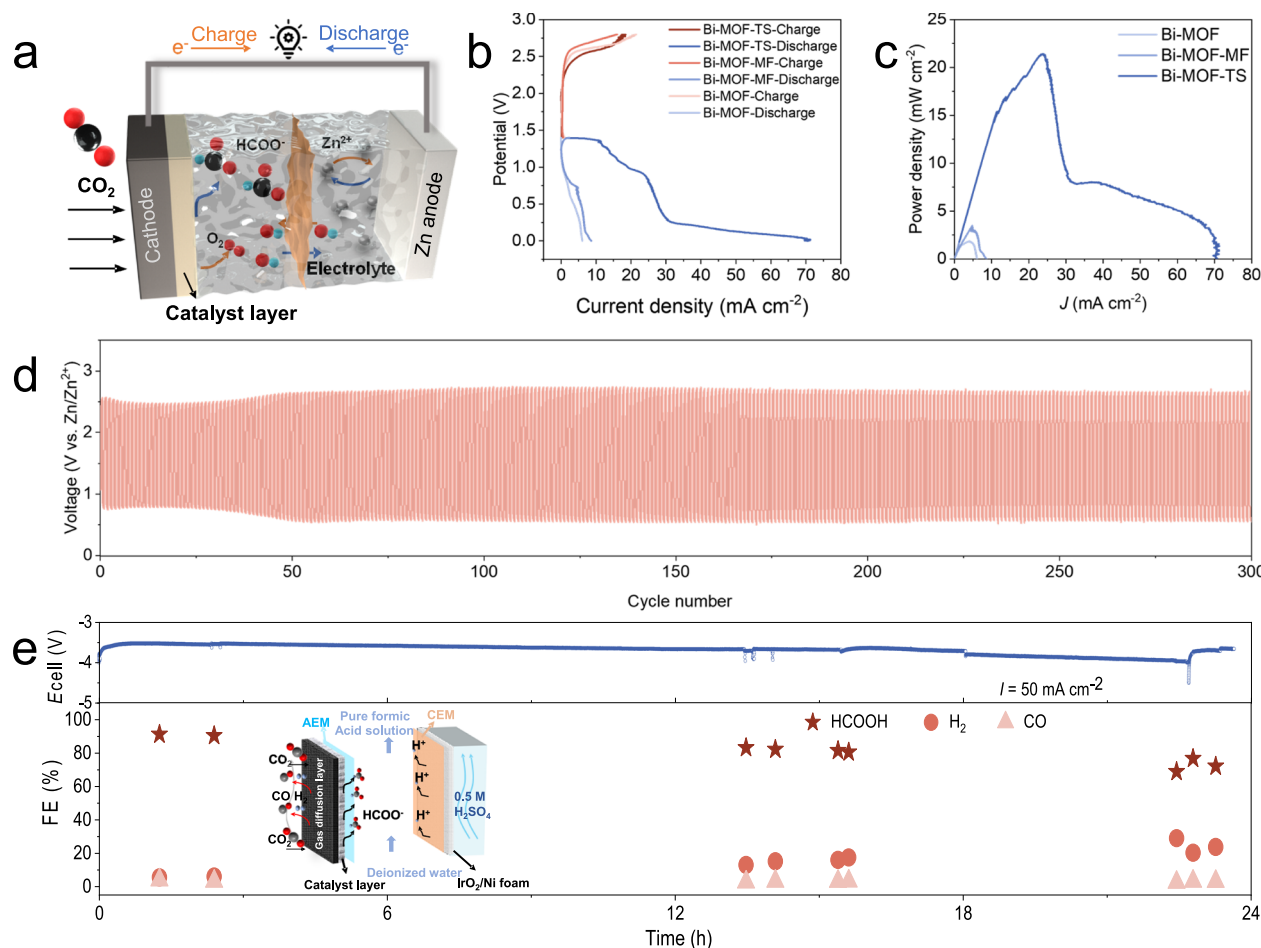
Fig. 7 | Zn-CO₂ battery and all-solid-state CO₂RR reactor performance. a Schematic of the Zn-CO₂ battery. **b** Charging and discharging curves of Bi-MOF, Bi-MOF-MF and Bi-MOF-TS. **c** The power density of the three catalysts. **d** Charge-discharge cycle curves at 2 mA cm⁻². **e** Long-term production of pure formic acid from Bi-MOF-TS at current densities of 50 mA cm⁻² in an all-solid-state reactor and a schematic of the all-solid-state reactor. Source data for Fig. 7b–e are provided as a Source Data file.

MOF-TS. Weaker Bi−O coordination strength led to a more dramatic electrochemical reconstruction process and produced more Bi vacancies on post-Bi⁰ catalysts. Appropriate tensile strain is generated on the surrounding sites of Bi vacancies and promotes the adsorption of the *OCHO intermediate. Since Bi clusters act as crystal nuclei to deposit Bi⁰ generated by electrochemical reduction, continuous vacancies like grain boundaries are generated, which generates greater tensile stress on surrounding sites. As a result, the Bi⁰ nanosheets derived from Bi-MOF-TS, which possess tensile strain over a larger area, exhibited a remarkably high FE for formate production, exceeding 95% across a wide potential range of 700 mV. Additionally, they achieved the highest formate partial current density recorded at −995 mA cm⁻². It is worth mentioning the performance of Bi-MOF-TS in acidic electrolyte, with a FE of 96 ± 0.64% for formic acid production at 400 mA cm⁻², and maintaining an efficiency of 87 ± 0.92% at 1000 mA cm⁻², highlights its good catalytic capability. The Zn-CO₂ battery employing the Bi-MOF-TS cathode demonstrates a high peak power density of 21.4 mW cm⁻² and exhibits stable rechargeability up to 300 cycles. Furthermore, it also shows continuous production of pure formic acid for 24 h. This work further elucidates the influence of Bi vacancies on adjacent sites and elucidates their unique role and superiority in the CO₂RR.

Methods
Chemicals
Bismuth nitrate pentahydrate (Bi(NO₃)₃·5H₂O) (99.9%), Benzene-1,3,5-tricarboxylic acid (C₉H₆O₆) (98%), Potassium bicarbonate (KHCO₃) (99.9%), Potassium hydroxide (KOH) (98%), Zinc diacetate

((CH₃COO)₂Zn) (99.99%) were purchased from Aladdin Industrial Inc. (Shanghai, China). Nafion solution (5 wt%) was purchased from Alfa Aesar Chemical Co. Analytical grade ethanol and methanol were purchased from Sinopharm Chemical Reagent Co., Ltd (Shanghai, China). All the chemicals were used without further purification.

Materials synthesis
Bi-MOF nanosheets. The synthesis of Bi-MOF was conducted using subsequent procedure. In a beaker, 150 mg Bi(NO₃)₃·5H₂O, 750 mg of Benzene-1,3,5-tricarboxylic acid, and 60 mL methanol were added in a beaker and thoroughly mixed using a vortex mixer. Then, the mixed solution was transferred into a Teflon vessel with a capacity of 100 mL. The vessel was sealed by an autoclave made of stain steel, which was then subjected to annealing at 120 °C for a duration of 24 h. Following this, the resulting powder of Bi-MOF nanosheets was washed multiple times with methanol, and subsequently, the sample was dried at 60 °C overnight.

Bi-MOF-MF. Bi-MOF-MF was synthesized by Bi-MOF powder after ball milling. The specific procedure is as follows. Bi-MOF nanosheets (400 mg) and 2 mL ethanol were added to a zirconia ball mill tank. The sample-to-ball weight ratio was 1:500 and rotary speed was 300 rpm for 1 h.

Bi-MOF-TS. Bi-MOF-TS was synthesized from Bi-MOF powder after Joule heat treatment (CIS-JH3.1, Hefei In-situ Technology. Co., Ltd). Bi-MOF nanosheets (10 mg) were placed onto a tungsten canoe, and then a thermal shock was carried out, the thermal shock time was 5 s, and the applied currency was 95 A.

Characterization

The phase analysis of catalysts was performed by D8 Advance X-ray diffractometer using Cu-Kα radiation ($\lambda = 1.5418$ Å). JEOL-7100F scanning electron microscope (SEM) and double spherical aberration-corrected transmission electron microscope (Titan Cubed Themis G2 300/Titan Cubed Themis G2 30) were adapted to perform the morphology, elemental distribution, and three-dimensional visualization of tomographic reconstruction of catalysts.

Electrochemical measurements

In order to control potential, the Autolab PGSTAT 204 electrochemical workstation was used in all electrochemical tests and all in-situ characterizations except Zn-CO₂ battery test. The CO₂RR performance of the catalysts prepared in this study was evaluated through a flow-cell reactor and stability test was employed in an all-solid-state MEA (Membrane Electrode Assembly) reactor. As for the flow-cell, 10 mg powder was dispersed in 1.9 mL ethanol and then 100 μL Nafion (5%) was added in the solution to obtain inks. The dispersion was then subjected to ultrasonication for 30 min. Then, the ink was uniformly sprayed onto a gas diffusion layer (GDL SGL 28BC) to yield the working electrode (2×5 cm²), with a 1 mg cm⁻² catalyst loading. The counter electrode was Ni foam, and the reference electrode was Ag/AgCl (SciKET, LEDONLAB) to calibrate the electric potential of counter electrode. An anion-exchange membrane (AEM, 1×1 cm², 50 μm thickness, Dioxide Materials Sustainion X37-50 grade 60) separates the working electrode (1×1 cm², the actual reaction area was 0.5×0.5 cm².) and counter electrode. The high-purity CO₂ (99.999%) used in all the tests was set at a flow rate of 50 sccm, and the electrolyte was 1 M KOH (pH = 14 ± 0.2) which was prepared by dissolving 56.11 g of KOH in distilled water, diluting to 1 L, and mixing thoroughly. The flow rate of high-purity CO₂ in our research was controlled by a gas flow meter (CS200, Beijing Sevenstar flow Co., Ltd). All potential values were adjusted to the RHE reference scale using the formula E(RHE) = E(Ag/AgCl) + 0.059 × pH + 0.198. The measured electrolyte resistance was 4.0 ± 0.5 Ω (Supplementary Fig. 49), we chose a 75% IR correction, which corresponds to 3 Ω.

In acidic system, working electrode was prepared same as that in alkaline system and Pt net (Nilaco, 99.95%) was served as counter electrode. A Nafion 117 membrane (1×1 cm², 183 μm thickness, Chemours, USA) was applied to separate working electrode and counter electrode. The electrolyte was 0.1 M K₂SO₄ + 0.02 M H₂SO₄ (pH = 1.5 ± 0.2). To prepare 0.1 M K₂SO₄ + 0.02 M H₂SO₄ solution, dissolved 17.43 g of K₂SO₄ in distilled water, added 1.11 mL of concentrated H₂SO₄, diluted to 1 L, and mix thoroughly. The Faradaic efficiencies and error bars for all products were calculated based on data from three independent experiments. No IR correction was applied during the testing process.

SPCE was also tested through a single experiment in acidic system. We regulated the flow rate of CO₂ from 50 to 1 sccm, and tested the CO₂RR performance at current density of 500 mA cm⁻². The measurements in neutral electrolyte were prepared same as that in acidic system, expect that the electrolyte was 1 M KHCO₃ (pH = 8.35 ± 0.3). Which was prepared by dissolving 100.12 g KHCO₃ in distilled water and then diluting to 1 L, mixing thoroughly. No IR correction was applied during the acidic and neutral systems testing process.

A flow-cell was used to assemble the Zn-CO₂ battery, with cathode prepared in the same manner as in alkaline system and polished Zn foil used as anode. Cathode electrolyte was 1 M KHCO₃ and anode electrolyte was 1 M KOH with 0.02 M (CH₃COO)₂Zn (pH = 14 ± 0.1), which were separated by a bipolar membrane (1×1 cm², 280 ± 30 μm thickness, FuMA-Tech GmbH, Germany). The 1 M KOH and 0.02 M (CH₃COO)₂Zn solution was prepared by dissolving 56.11 g of KOH and 3.67 g of (CH₃COO)₂Zn in distilled water, followed by dilution to a final volume of 1 L and thorough mixing. The cathode received a supply of CO₂ gas with 50 sccm flow rate. Neware battery test system (CT-4008,

Shenzhen, China) was used to test the cycling performance. The test was carried out at room temperature.

The all-solid-state MEA reactor, was applied to produce pure HCOOH solution. A Nafion membrane (Fuel Cell Store) and an AEM (Dioxide Materials) were used for cation and anion exchange, respectively. Twenty-five milligrams powder was dispersed in 4.75 mL ethanol and then 250 μL Nafion was added in the solution to obtain inks. After ultrasonic homogenization, the ink was sprayed onto a 5×10 cm² YLS-30T gas diffusion layer (GDL) electrode with a loading density of catalyst ~0.5 mg cm⁻². The reaction area in the all-solid-state MEA reactor was 4.0 cm². For the anode, IrO₂ (Aladdin, 99.9%) was loaded onto a titanium mesh. The cathode received a supply of CO₂ gas with 30 sccm flow rate that was humidified. For the stability test, the flow rate was reduced to 20 sccm 0.5 M H₂SO₄ circulated on the anode side at rate of 2 mL min⁻¹. A solid ion conductor made of porous styrene-divinylbenzene sulfonated copolymer was employed. To facilitate the release of the generated HCOOH from the solid-state electrolyte layer, DI water was employed with a flow rate of 1.4 mL min⁻¹. Which was 0.6 mL min⁻¹ during stability test.

Ten milligrams of catalysts were separated in 0.8 mL ethanol, 0.1 mL H₂O, and 0.1 mL Nafion solution to obtain inks. The electrodes used for the electrochemical surface area (ECSA) test were prepared through doping 10 μL inks on glassy-carbon electrode (GCE, diameter = 0.5 cm). The ECSA test of electrocatalysts was determined by performing CV in the potential range of 0.05 to −0.03 V vs. RHE at different scan rates of 10, 20, 30, 40, 50, 60, 70, 80, 90, and 100 mV s⁻¹. The slope was calculated by the following formula:

$$\Delta j = (j_a - j_c)/2 \tag{1}$$

Where j_a and j_c represent the anodic and cathodic current densities of catalysts at 0.01 V vs. RHE, respectively.

All electrolytes mentioned above were sealed and stored in volumetric flasks at room temperature, and used within 1 week.

Reduction product analysis

A thermal conductivity detector (TCD) was used to detect C1 gaseous products and flame ionization detector (FID) was utilized to detect H₂ by online GC (GC2014C, Shimadzu). An analysis time of 7 min was set for every gas phase product. The FEs for gas products, including H₂ and CO, were calculated using the following formula:

$$FE(\%) = \frac{NF \times (\frac{\nu}{60}) \times (\frac{y}{24.5 \times 10^9})}{i} \times 100\% \tag{2}$$

Here, N represents the number of electrons needed for the products, v (sccm) is the gas flow rate, y (ppm) is the volume concentration of the gas reduce product, the Faraday constant (96,500 C mol⁻¹) is represented by F, and i (A) is the collected cell current.

The single-pass CO₂ conversion efficiency is calculated as follows:

$$SPCE = \frac{(j_{product} \times 60s)/(n \times F)}{(v \times 1min)/V_m} \tag{3}$$

Where $j_{product}$ is partial current (A) of CO₂RR product, n is electron transfer for the formation of each product molecule, V_m is 24.51 mol⁻¹.

The energy efficiency is calculated as follows:

$$EE_{full-cell} = \frac{(1.23 + (-E_{formicacid})) \times FE_{formicacid}}{-E_{full-cell}} \tag{4}$$

Where the $E_{full-cell}$ represents the cell voltage utilized within the solid-state reactor, whereas the $E_{formic\ acid}$ has a value of −0.2 V.

NMR (Bruker Avance III, 600 M) was used to quantify liquid products by analyzing the collected electrolytes. The interior label was

dimethyl sulfoxide (DMSO) with a known concentration. Utilizing 1H NMR analysis, the quantification of product amounts was conducted by assessing the relative peak area of $HCOO^-$ at 7.09 ppm and DMSO at 2.6 ppm. The FE for $HCOO^-$ was computed using the subsequent formula:

$$FE(\%) = \frac{nNF}{Q} \times 100\% \qquad (5)$$

Here, the amount of $HCOO^-$ (mol) measured is represented by n, N represents the number of electrons needed for each reduction product, the Faraday constant (96,500 C mol^{-1}) is represented by F, and Q denotes the overall charge recorded throughout the operation process.

In-situ ATR-SEIRAS measurements

An FT-IR spectrometer (Nicolet iS50, Thermo Scientific) equipped with an MCT-A detector was used to acquire the in-situ ATR-SEIRAS spectra (Supplementary Fig. 50). To prepare the inks, 10 mg catalyst powder was scattered in the solution which was consisted of 0.9 mL of ethanol and 0.1 mL of Nafion solution. In other in-situ characterizations, the approach of prepared inks was same as in it. The dispersion was then subjected to ultrasonication for 30 min. A hemicylindrical Si prism with a chemically deposited Au film (-1 cm^2) had 5 µL of ink applied on it, yielding a catalyst loading of 0.05 mg cm^{-2}. In a spectro-electrochemical cell, we used a Pt foil (1 × 1 cm) counter electrode, an Ag/AgCl reference electrode (CHI111, Shanghai Yueci Electronic Co.), and 0.1 M $KHCO_3$ (pH = 8.2 ± 0.1) solution as the electrolyte. Each single-beam spectrum was scanned 240 times. The spectra collecting resolution was 4 cm^{-1}. During the reaction, high pure CO_2 was continuously introduced into the electrolyte. 0.1 M $KHCO_3$ was prepared by dissolving 10.01 g $KHCO_3$ in distilled water and then diluting to 1 L, mixing thoroughly.

In-situ X-ray absorption measurements

The Bi L_3-edge XANES and EXAFS spectra were collected in fluorescence excitation mode at room temperature at beamline 12BM for synchrotron radiation from Advanced Photon Source and Beamline BL11B at the Shanghai Synchrotron Radiation Facility (SSRF). For the electrochemical reaction, a commercially available electrolytic cell (Zhongkewanheng) was employed. The working electrode was prepared using the same method employed for the flow cell. The electrolyte used was 0.1 M $KHCO_3$ solution saturated with CO_2. The counter electrode was made of Pt foil (1 × 1 cm), while Ag/AgCl (CHI111, Shanghai Yueci Electronic Co.) served as the reference electrode. Signal collection was carried out by performing a chronoamperometry test at the desired potential for a duration of 10 min.

In-situ Raman measurements

Raman spectra were collected by a Horiba LabRAM HR Evolution with a He/Ne laser of λ = 532 nm and 4.9 mW in a customized Teflon cell (Supplementary Fig. 51). The electrolyte was CO_2-filled 0.1 M $KHCO_3$. A working electrode consisting of a catalyst-supported gold electrode (GE) with a diameter of 0.3 cm was utilized. In this characterization, we used an Ag/AgCl reference electrode (CHI111, Shanghai Yueci Electronic Co.), and counter electrode was a Pt wire (Φ1 mm × 37 mm). The preparation process for the electrocatalyst ink followed the same procedure as described earlier. Subsequently, on a freshly polished GE, 5 µL ink was evenly dropped.

DFT calculations

All first-principles DFT calculations were conducted using the Vienma ab initio simulation package[68,69]. It adopts the generalized gradient approximation in the Perdew−Burke−Ernzerhof functional (GGA-PBE)[70] to treat the electron exchange and correlation interaction while utilizing the projector-augmented wave method[71] to describe the ion-electron interactions[72]. We applied a plane-wave basis set with a kinetic energy cut-off of 450 eV to perform the calculations. The DFT-D3 method developed by Grimme et al. was employed to describe the long-range dispersion interaction. The k-point sampling of a (2 × 2 × 1) mesh within the Monkhorst−Pack scheme is utilized for optimization[73]. The calculations for optimization were completed when the electronic self-consistent iteration and force were reached 0.02 eV $Å^{-1}$ and 10^{-5} eV, respectively.

For the modeling of Pure Bi, Bi-1SV, Bi-2SV, and Bi-3SV, we built a monolayer Bi slab within a lattice cell of 36.47 × 31.59 $Å^2$, which contains 128 Bi atoms. The successive removal of single Bi atoms to construct Bi-1SV, Bi-2SV, and Bi-3SV. The free energy is calculated based on $\Delta G = \Delta E + \Delta EZPE - T\Delta S$, where ΔE represents the energy change which was computed through DFT calculations. $\Delta EZPE$ refers to the difference in zero-point energies between the adsorbed state and gas phase, which was calculated by summing the vibrational frequencies for all models using the equation: $EZPE = 1/2\sum hvi$ (where T is the temperature, set at 298.15 K in the reaction system). ΔS represents the difference in entropies between the adsorbed state and gas phase. In addition, the energy of the proton/electron pair is equal to half the energy of hydrogen molecule according to the computational hydrogen electrode method[72].

Data availability

All data supporting the findings of this study are available within the article and the Supplementary Information file. The source data of the figures and atomic coordinates of optimized computational models are available on Figureshare (DOI:10.6084/m9.figshare.28148366).[74] Source data are provided with this paper.

References

1. De Luna, P. et al. What would it take for renewably powered electrosynthesis to displace petrochemical processes? *Science* **364**, eaav3506 (2019).
2. Bushuyev, O. S. et al. What should we make with CO_2 and how can we make it? *Joule* **2**, 825–832 (2018).
3. Wang, G. et al. Electrocatalysis for CO_2 conversion: from fundamentals to value-added products. *Chem. Soc. Rev.* **50**, 4993–5061 (2021).
4. Zhang, Z., Zhu, J., Chen, S., Sun, W. & Wang, D. Liquid fluxional Ga single atom catalysts for efficient electrochemical CO_2 reduction. *Angew. Chem. Int. Edit.* **62**, e202215136 (2023).
5. Quan, Y., Zhu, J. & Zheng, G. Electrocatalytic reactions for converting CO_2 to value-added products. *Small Sci.* **1**, 2100043 (2021).
6. Li, G. et al. Direct plasma phosphorization of Cu foam for Li ion batteries. *J. Mater. Chem. A* **8**, 16920–16925 (2020).
7. Birdja, Y. Y. et al. Advances and challenges in understanding the electrocatalytic conversion of carbon dioxide to fuels. *Nat. Energy* **4**, 732–745 (2019).
8. Chen, C., Kotyk, J. F. K. & Sheehan, S. W. Progress toward commercial application of electrochemical carbon dioxide reduction. *Chem* **4**, 2571–2586 (2018).
9. Zhu, J. et al. Advances and challenges in single-site catalysts towards electrochemical CO_2 methanation. *Energy Environ. Sci.* **16**, 4812–4833 (2023).
10. Jiang, K. et al. Isolated Ni single atoms in graphene nanosheets for high-performance CO_2 reduction. *Energy Environ. Sci.* **11**, 893–903 (2018).
11. Jin, S., Hao, Z., Zhang, K., Yan, Z. & Chen, J. Advances and challenges for the electrochemical reduction of CO_2 to CO: from fundamentals to industrialization. *Angew. Chem. Int. Edit.* **133**, 20795–20816 (2021).
12. Zhongming, Z., Linong, L., Xiaona, Y., Wangqiang, Z. & Wei, L. N-bridged Co-N-Ni: new bimetallic sites for promoting electrochemical CO_2 reduction. *Energy Environ. Sci.* **14**, 3019–3028 (2021).

13. Hu, Q. et al. Facile synthesis of sub-nanometric copper clusters by double confinement enables selective reduction of carbon dioxide to methane. *Angew. Chem. Int. Edit.* **59**, 19054–19059 (2020).

14. Zhao, J. et al. Modulation of *CH$_x$O adsorption to facilitate electrocatalytic reduction of CO_2 to CH_4 over Cu-based catalysts. *J. Am. Chem. Soc.* **145**, 6622–6627 (2023).

15. Chen, S. et al. Engineering water molecules activation center on multisite electrocatalysts for enhanced CO_2 methanation. *J. Am. Chem. Soc.* **144**, 12807–12815 (2022).

16. Jiang, Z. et al. Discovery of main group single Sb–N$_4$ active sites for CO_2 electroreduction to formate with high efficiency. *Energy Environ. Sci.* **13**, 2856–2863 (2020).

17. Wu, Z. et al. Engineering bismuth–tin interface in bimetallic aerogel with a 3D porous structure for highly selective electrocatalytic CO_2 reduction to HCOOH. *Angew. Chem. Int. Edit.* **133**, 12662–12667 (2021).

18. Zheng, T. et al. Copper-catalysed exclusive CO_2 to pure formic acid conversion via single-atom alloying. *Nat. Nanotechnol.* **16**, 1386–1393 (2021).

19. Zheng, X. et al. Sulfur-modulated tin sites enable highly selective electrochemical reduction of CO_2 to formate. *Joule* **1**, 794–805 (2017).

20. Shen, H. et al. Acidic CO_2-to-HCOOH electrolysis with industrial-level current on phase engineered tin sulfide. *Nat. Commun.* **14**, 2843 (2023).

21. Li, F. et al. Molecular tuning of CO_2-to-ethylene conversion. *Nature* **577**, 509–513 (2020).

22. Ma, Y. et al. Confined growth of silver–copper janus nanostructures with {100} facets for highly selective tandem electrocatalytic carbon dioxide reduction. *Adv. Mater.* **34**, 2110607 (2022).

23. Zhang, W. et al. A typical oxygen-bearing copper boosts ethylene selectivity toward electrocatalytic CO_2 reduction. *J. Am. Chem. Soc.* **142**, 11417–11427 (2020).

24. Xia, W. et al. Adjacent copper single atoms promote C–C coupling in electrochemical CO_2 reduction for the efficient conversion of ethanol. *J. Am. Chem. Soc.* **145**, 17253–17264 (2023).

25. Zhu, J. et al. Surface passivation for highly active, selective, stable, and scalable CO2 electroreduction. *Nat. Commun.* **14**, 4670 (2023).

26. Wang, W. et al. Carburized In$_2$O$_3$ nanorods endow CO_2 electroreduction to formate at 1 A cm^{-2}. *ACS Catal.* **13**, 796–802 (2022).

27. Lamagni, P. et al. Restructuring metal–organic frameworks to nanoscale bismuth electrocatalysts for highly active and selective CO_2 reduction to formate. *Adv. Funct. Mater.* **30**, 1910408 (2020).

28. Zhang, E. et al. Bismuth single atoms resulting from transformation of metal–organic frameworks and their use as electrocatalysts for CO_2 reduction. *J. Am. Chem. Soc.* **141**, 16569–16573 (2019).

29. Cao, C. et al. Metal–organic layers leading to atomically thin bismuthene for efficient carbon dioxide electroreduction to liquid fuel. *Angew. Chem. Int. Edit.* **59**, 15014–15020 (2020).

30. Deng, P. et al. Bismuth oxides with enhanced bismuth–oxygen structure for efficient electrochemical reduction of carbon dioxide to formate. *ACS Catal.* **10**, 743–750 (2019).

31. Gilbert, B., Huang, F., Zhang, H., Waychunas, G. A. & Banfield, J. F. Nanoparticles: strained and stiff. *Science* **305**, 651–654 (2004).

32. Liu, H. et al. Observation on microenvironment changes of dynamic catalysts in acidic CO_2 reduction. *J. Am. Chem. Soc.* **146**, 5333–5342 (2024).

33. Lhostis, F. et al. Promoting selective CO_2 electroreduction to formic acid in acidic medium with low potassium concentrations under high CO_2 pressure. *Chem. Electro. Chem.* **11**, e202300799 (2024).

34. Luo, M. & Guo, S. Strain-controlled electrocatalysis on multimetallic nanomaterials. *Nat. Rev. Mater.* **2**, 1–13 (2017).

35. Potapenko, D. V., Li, Z., Kysar, J. W. & Osgood, R. M. Nanoscale strain engineering on the surface of a bulk TiO$_2$ crystal. *Nano Lett.* **14**, 6185–6189 (2014).

36. Castellanos-Gomez, A. et al. Local strain engineering in atomically thin MoS$_2$. *Nano Lett.* **13**, 5361–5366 (2013).

37. Du, M., Cui, L., Cao, Y., & Bard, AJ. Mechanoelectrochemical catalysis of the effect of elastic strain on a platinum nanofilm for the ORR exerted by a shape memory alloy substrate. *J. Am. Chem. Soc.* **137**, 7397–7403 (2015).

38. Wang, H. et al. Direct and continuous strain control of catalysts with tunable battery electrode materials. *Science* **354**, 1031–1036 (2016).

39. Li, Y. et al. Enhancing local CO_2 adsorption by L-histidine incorporation for selective formate production over the wide potential window. *Angew. Chem. Int. Edit.* **62**, e202313522 (2023).

40. Li, F. et al. Highly stable two-dimensional bismuth metal-organic frameworks for efficient electrochemical reduction of CO_2. *Appl. Catal. B Environ.* **277**, 119241 (2020).

41. Huang, J. E. et al. CO_2 electrolysis to multicarbon products in strong acid. *Science* **372**, 1074–1078 (2021).

42. Hao, Y.-C. et al. Promoting nitrogen electroreduction to ammonia with bismuth nanocrystals and potassium cations in water. *Nat. Catal.* **2**, 448–456 (2019).

43. Duan, J. et al. Active and conductive layer stacked superlattices for highly selective CO_2 electroreduction. *Nat. Commun.* **13**, 2039 (2022).

44. Tang, S.-F. et al. Decorating graphdiyne on ultrathin bismuth subcarbonate nanosheets to promote CO_2 electroreduction to formate. *Sci. Bull.* **66**, 1533–1541 (2021).

45. Chen, M. et al. In-situ/operando Raman techniques for in-depth understanding on electrocatalysis. *Chem. Eng. J.* **461**, 141939 (2023).

46. Zhang, W. et al. Dynamic restructuring of coordinatively unsaturated copper paddle wheel clusters to boost electrochemical CO_2 reduction to hydrocarbons. *Angew. Chem. Int. Edit.* **61**, e202112116 (2022).

47. Yao, D. et al. The controllable reconstruction of Bi-MOFs for electrochemical CO_2 reduction through electrolyte and potential mediation. *Angew. Chem. Int. Edit.* **133**, 18326–18332 (2021).

48. Xia, Z. & Guo, S. Strain engineering of metal-based nanomaterials for energy electrocatalysis. *Chem. Soc. Rev.* **48**, 3265–3278 (2019).

49. Fan, L. et al. Biaxially compressive strain in Ni/Ru core/shell nanoplates boosts Li–CO_2 batteries. *Adv. Mater.* **34**, 2204134 (2022).

50. Luo, M. et al. PdMo bimetallene for oxygen reduction catalysis. *Nature* **574**, 81–85 (2019).

51. Zhong, H. et al. Synergistic electroreduction of carbon dioxide to carbon monoxide on bimetallic layered conjugated metal-organic frameworks. *Nat. Commun.* **11**, 1409 (2020).

52. Zhu, J. et al. Ultrahigh stable methanol oxidation enabled by a high hydroxyl concentration on Pt clusters/MXene interfaces. *J. Am. Chem. Soc.* **144**, 15529–15538 (2022).

53. Firet, N. J. & Smith, W. A. Probing the reaction mechanism of CO_2 electroreduction over Ag films via operando infrared spectroscopy. *ACS Catal.* **7**, 606–612 (2017).

54. Zhu, S., Jiang, B., Cai, W.-B. & Shao, M. Direct observation on reaction intermediates and the role of bicarbonate anions in CO_2 electrochemical reduction reaction on Cu surfaces. *J. Am. Chem. Soc.* **139**, 15664–15667 (2017).

55. Morlanes, N., Takanabe, K. & Rodionov, V. Simultaneous reduction of CO_2 and splitting of H_2O by a single immobilized cobalt phthalocyanine electrocatalyst. *ACS Catal.* **6**, 3092–3095 (2016).

56. Hu, X.-M. et al. Selective CO_2 reduction to CO in water using earth-abundant metal and nitrogen-doped carbon electrocatalysts. *ACS Catal.* **8**, 6255–6264 (2018).

57. Fan, K. et al. Curved surface boosts electrochemical CO_2 reduction to formate via bismuth nanotubes in a wide potential window. *ACS Catal.* **10**, 358–364 (2019).

58. Wang, T. et al. Gas diffusion strategy for inserting atomic iron sites into graphitized carbon supports for unusually high-efficient CO_2 electroreduction and high-performance Zn–CO_2 batteries. *Adv. Mater.* **32**, 2002430 (2020).

59. Yan, S. et al. Electron localization and lattice strain induced by surface lithium doping enable ampere-level electrosynthesis of formate from CO_2. *Angew. Chem. Int. Edit.* **133**, 25945–25949 (2021).

60. Xie, J. et al. Reversible aqueous Zinc–CO_2 batteries based on CO_2–HCOOH interconversion. *Angew. Chem. Int. Edit.* **57**, 16996–17001 (2018).

61. Zeng, Z. et al. Orbital coupling of hetero-diatomic nickel-iron site for bifunctional electrocatalysis of CO_2 reduction and oxygen evolution. *Nat. Commun.* **12**, 4088 (2021).

62. Li, Z. et al. Elucidation of the synergistic effect of dopants and vacancies on promoted selectivity for CO_2 electroreduction to formate. *Adv. Mater.* **33**, 2005113 (2021).

63. Ozden, A. et al. High-rate and efficient ethylene electrosynthesis using a catalyst/promoter/transport layer. *ACS Energy Lett.* **5**, 2811–2818 (2020).

64. Lees, E. W., Mowbray, B. A. W., Parlane, F. G. L. & Berlinguette, C. P. Gas diffusion electrodes and membranes for CO_2 reduction electrolysers. *Nat. Rev. Mater.* **7**, 55–64 (2022).

65. Ozden, A. et al. Carbon-efficient carbon dioxide electrolysers. *Nat. Sustain.* **5**, 563–573 (2022).

66. Zheng, T. et al. Upcycling CO_2 into energy-rich long-chain compounds via electrochemical and metabolic engineering. *Nat. Catal.* **5**, 388–396 (2022).

67. Kim, J. Y. T. et al. Recovering carbon losses in CO_2 electrolysis using a solid electrolyte reactor. *Nat. Catal.* **5**, 288–299 (2022).

68. Kresse, G. & Hafner, J. Ab initio molecular-dynamics simulation of the liquid-metal–amorphous-semiconductor transition in germanium. *Phys. Rev. B* **49**, 14251 (1994).

69. Kresse, G. & Furthmüller, J. Efficient iterative schemes for ab initio total-energy calculations using a plane-wave basis set. *Phys. Rev. B* **54**, 11169 (1996).

70. Perdew, J. P., Burke, K. & Ernzerhof, M. Generalized gradient approximation made simple. *Phys. Rev. Lett.* **77**, 3865 (1996).

71. Blöchl, P. E. Projector augmented-wave method. *Phys. Rev. B* **50**, 17953 (1994).

72. Grimme, S., Antony, J., Ehrlich, S. & Krieg, H. A consistent and accurate ab initio parametrization of density functional dispersion correction (DFT-D) for the 94 elements H-Pu. *J. Chem. Phys.* **132**, 15 (2010).

73. Monkhorst, H. J. & Pack, J. D. Special points for Brillouin-zone integrations. *Phys. Rev. B* **13**, 5188 (1976).

74. Chen, X. Activating inert non-defect sites in Bi catalysts using tensile strain engineering for highly active CO_2 electroreduction. figshare https://doi.org/10.6084/m9.figshare.28148366 (2025).

Acknowledgements

Author contributions

Competing interests

Additional information

Supplementary information The online version contains supplementary material available at https://doi.org/10.1038/s41467-025-56975-8.

Correspondence and requests for materials should be addressed to Wen Luo, Jiexin Zhu, Ziyun Wang or Liqiang Mai.

Peer review information *Nature Communications* thanks Antonia Herzog, and the other, anonymous, reviewer(s) for their contribution to the peer review of this work. A peer review file is available.

Reprints and permissions information is available at http://www.nature.com/reprints

Publisher's note Springer Nature remains neutral with regard to jurisdictional claims in published maps and institutional affiliations.